IEEE Access
Multidisciplinary | Rapid Review | Open Access Journal

Received February 15, 2019, accepted February 27, 2019, date of publication March 8, 2019, date of current version May 22, 2019.

Digital Object Identifier 10.1109/ACCESS.2019.2902975

Fast High-Precision Electrical Impedance Tomography System for Real-Time Perfusion Imaging

WEICHEN LI[1], JUNYING XIA[1], GE ZHANG[2], HANG MA[1], BENYUAN LIU[1], LIN YANG[3], YIMIN ZHOU[1], XIUZHEN DONG[1], (Member, IEEE), FENG FU[1], AND XUETAO SHI[1]

[1]Faculty of Biomedical Engineering, Fourth Military Medical University, Xi'an, China
[2]Department of Radiology, Bethune International Peace Hospital, Shijiazhuang, China
[3]Department of Aerospace Medicine, Fourth Military Medical University, Xi'an, China

Corresponding author: Xuetao Shi (shixuetao@fmmu.edu.cn)

This work was supported in part by the National Natural Science Foundation of China under Grant 61571445, in part by the National Natural Science Foundation of China under Grant 51837011, in part by the Major Scientific Research Program under Grant ALJ17J001, in part by the Major Basic Research Program of Shaanxi Province of China under Grant 2016ZDJC14, in part by the Medical Promotion Plan of Fourth Military Medical University under Grant 2016TSB-016, and in part by the Shaanxi Province Science and Technology Program under Grant 2016SF-258.

ABSTRACT Periodical changes in bioimpedance caused by blood perfusion are relatively fast and weak; therefore, a fast, high-precision imaging system is required. A novel electrical impedance tomography (EIT) system is proposed for real-time perfusion imaging. Synchronous parallel sampling is combined with timely excitation switching control to achieve fast acquisition and maintain high sampling accuracy. To further improve the overall precision of the system, a bipolar-mirror feedback voltage controlled current source and an internal calibration unit was used to improve the current precision and measurement accuracy, respectively. Test results of the resistor model show that the system has a signal-to-noise ratio of 81 dB at 50 kHz and achieves an imaging rate of 100 frames/ s. A preliminary test shows that the reconstructed EIT images reveal a complete cycle of blood exchange between the heart and lungs. Our system may provide a useful research platform for real-time and non-invasive blood perfusion imaging, which could be used in *in vivo* studies.

INDEX TERMS Impedance measurement, data acquisition, tomography.

I. INTRODUCTION

Blood perfusion is a physiological phenomenon in which blood flows through the vascular network and delivers oxygen and nutrients to tissue cells. All organ tissues require adequate blood supply to ensure proper functioning [1], which has essential clinical guiding value for the diagnosis of diseases such as pulmonary embolism [2], moyamoya disease [3], and related treatments (e.g., lung transplantation [4] and carotid stripping [5]).

Modern perfusion imaging techniques such as magnetic resonance imaging (MRI) [6], computed tomography (CT) perfusion imaging [7], and positron emission CT [8] feature high spatial resolution imaging. They have a wide range of applications in clinical and have become routine testing methods in clinical practice [9]. However, these technologies have the disadvantages of large equipment size, long detection period, complicated inspection process, high cost of use, and harsh environment requirements. Moreover, they can be harmful to the human body and cannot meet the requirements of real-time dynamic blood perfusion imaging, resulting in the loss of a large amount of physiological information. Therefore, realizing real-time blood perfusion imaging remains one of the most critical requirements of further diagnosis and treatment of blood perfusion-related diseases, an urgent problem in clinical practice.

Electrical impedance tomography (EIT) is a relatively new imaging technique with several advantages, including high temporal-resolution, high impedance-sensitivity, good safety, and noninvasiveness. The technique uses surface electrodes to apply the excitation signal and detects response signals on the measuring electrodes. Image reconstruction of the target internal resistivity or its variation distribution can be achieved by solving the inverse problem of the

The associate editor coordinating the review of this manuscript and approving it for publication was Chao Tan.

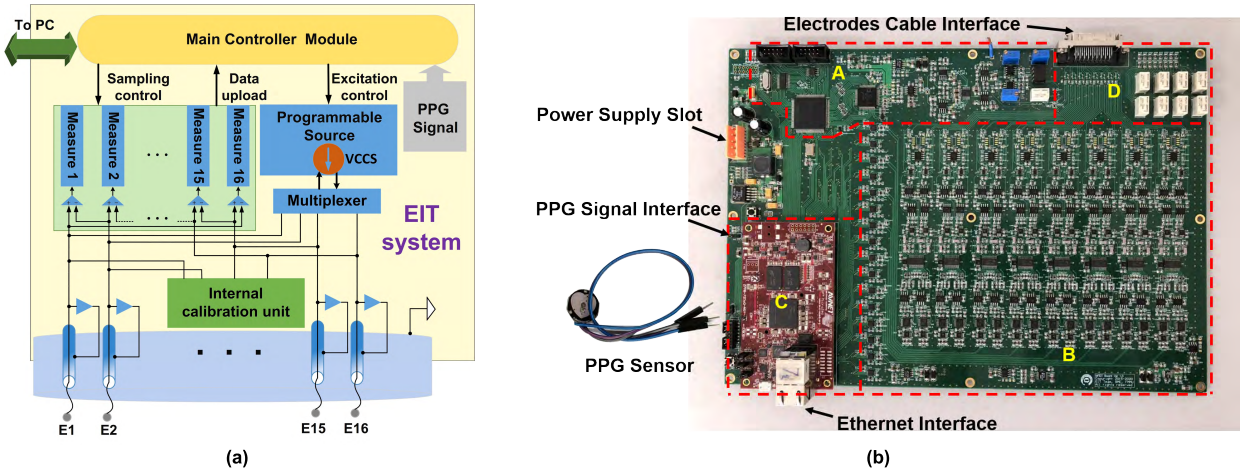

FIGURE 1. Overview of system architecture. (a) Overall structure diagram. (b) Photo of the system printed circuit board (PCB), in which capital letters represent: A: excitation source module, B: signal measurement module, C: main control module, and D: internal calibration circuit.

electromagnetic field [10], which is expected to fill the gap in dynamic clinical disease monitoring [11]. Given the significant differences between the bioimpedance characteristics of blood and other tissues [12], [13], the EIT system is expected to achieve dynamic blood perfusion imaging.

The perfusion EIT signal is mainly composed of the basic tissue impedance Z_0 and the dynamically changing perfusion impedance ΔZ. The amplitude of ΔZ is at least an order of magnitude smaller than that of Z_0 [14], [15], which means that a higher precision of the system may be required. Furthermore, the ΔZ signal is a periodical fast-changing signal contains substantial information, which has the same cycle with the cardiac. Leonhardt showed that an EIT system for perfusion imaging should have a higher sampling rate [16]. Several research groups have developed EIT systems for perfusion imaging. GOE-MF II, designed by Hahn [17], was used to study the ventilation and cardiac related impedance changes with a frame rate of 44Hz [18]; McCann developed a system named fEITER for perfusion research with a sampling frequency up to 100 fps [19]. A preliminary study on the frequency response of cardiac activities was conducted by Zhou, and the system can ensure a high signal-to-noise ratio (SNR) of 80 dB with a scanning speed of 20 fps [20]. However, since physiological changes occur during data collection, Yerworth deemed that such an effect will cause some blurring of the temporal information [21]. Therefore, the actual signal sampling time should be as short as possible. In summary, although existing EIT data acquisition systems can detect blood perfusion to a certain extent, there may be either insufficient precision, or ignorance of the impact on long sampling time in a single frame, which might not facilitate in-depth perfusion imaging detection.

Here, a fast and high-precision EIT system is presented to meet the following goals. (1) Sampling time: To acquire the precise data from even neonatal human subjects, Yerworth deemed that the actual sampling time of each frame should not exceed 8 ms [22]. (2) Acquisition precision: The design goal of the system is to study perfusion detection in multiple organs. Since cerebral blood perfusion may be the weakest area of organ perfusion, and the relative average variation measured of the rheoencephalography signal is only 0.146% [23], the acquisition precision of this system should be better than 0.05%.

II. SYSTEM DESIGN

As shown in Fig. 1, the system was mainly based on a high-precision acquisition system [24] that used 16 electrodes for imaging. A semi-parallel structure, mainly consisting of a single excitation source and 16 parallel measurement channels, was adopted. Under the control of the main control module, the excitation source generates a precise voltage signal using digital synthesis technology and converts it into an excitation current signal via a voltage controlled current source (VCCS); the multiplexer injects current into different pairs of excitation electrodes by configuration, and all channels simultaneously complete the measurement of the adjacent channels' boundary voltages; The FPGA of the MicroZed (Xilinx, USA) in the main control module is utilized to demodulate the modulus and phase information of the processed digital data from measurement channels immediately. The orthogonal sequence digital demodulation method was adopted to realize better suppression of random noise in the demodulated signal [25]. A photoplethysmography (PPG) sensor was utilized to collect the heart rate signal.

In this study, to further improve the overall precision of the system, bipolar mirror feedback VCCS was used to reduce the common-mode error of the excitation current signal, and an internal calibration unit was added to reduce the measurement errors. To achieve fast acquisition, timely excitation switching control was proposed to ensure that the system's acquisition process is not subject to excessive delay due to transient response. Meanwhile, combined with the scheme of synchronous parallel sampling and on-chip demodulation,

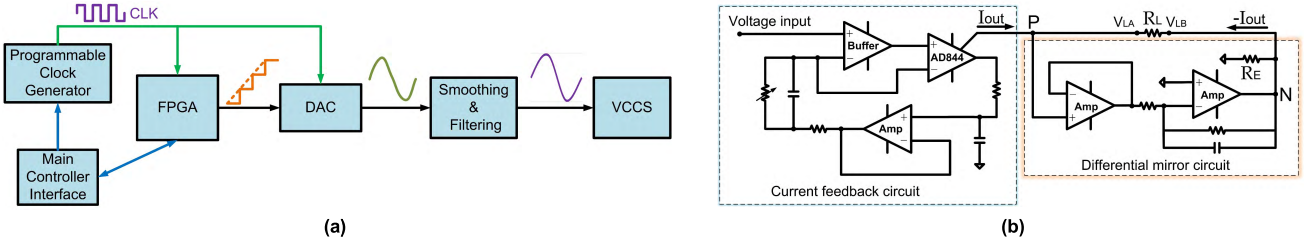

FIGURE 2. Excitation source design. (a) Block diagram of the basic unit of programmable excitation source digital synthesis [24]. (b) Schematic of the voltage controlled current source (VCCS) circuit.

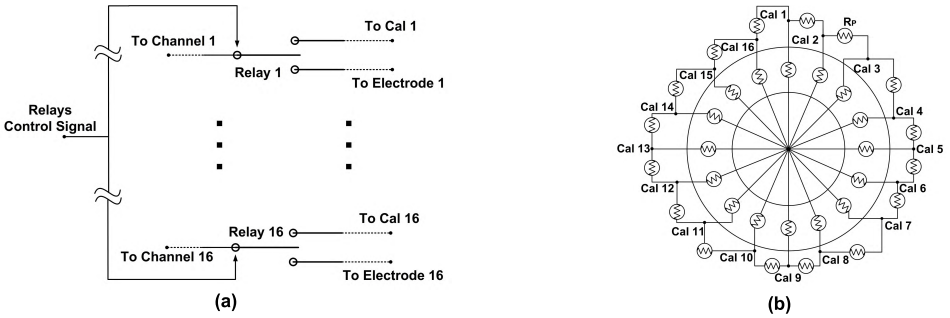

FIGURE 3. Schematic diagram of the internal calibration circuit. (a) Scheme of the switches network. (b) Topology of the precision resistors model.

the system can have a high sampling rate with high sampling accuracy.

A. BIPOLAR-MIRROR FEEDBACK VCCS

Current sources in most systems typically release the excitation current by connecting the negative excitation electrode to ground directly [26]–[29], which induces high common-mode voltage errors [30]. As the differential mirror circuit can form a floating structure at the ends of the load and improve the noise suppression ability [31], the excitation source used in this system is designed as shown in Fig. 2(a), which mainly consists of a precise voltage signal generating circuit and a VCCS circuit. The digital synthesis basic unit proposed by Shi *et al.* [24] was used to synthesize the high-precision sinusoidal voltage signal. The VCCS circuit designed in this work is composed of a current feedback circuit and a differential mirror circuit [32].

From Fig. 2(b), the differential mirror circuit consists of a voltage follower followed by an inverting amplifier. A resistor R_E for absorbing residual current signals due to the imbalance of two ends is introduced into the circuit. Thus, a bipolar-mirror feedback current source (BMFCS) is constructed. The voltage signals V_{LA} and V_{LB} are equal in amplitude and have a 180° phase difference when the two ends of the load R_L are matched. The common-mode signal V_{CM} of the current source was defined as:

$$V_{CM} = \frac{1}{2}(V_A + V_B). \tag{1}$$

Thus, the common-mode signal should theoretically be zero, thereby increasing the SNR of the output current signal.

B. INTERNAL CALIBRATION

The systematic error of the semi-parallel system is mainly manifested by the gain and phase error of each measurement channel and inconsistency between the channels [33]. As the excitation frequency increases, the shunting problem caused by the rise of stray capacitance in the system devices, circuit wiring, and electrode leads, inevitably introduces these errors, making it challenging to analyze impedance information within the imaging target accurately [34]. Therefore, an internal calibration unit was designed to calibrate these errors. As shown in Fig. 3(a), the switching circuit controls the access of the measurement object through 16 single pole-double throw relays, and the relays have low switching capacitance and low on-resistance. The calibration resistor network has the same topology reported by Oh *et al.* [35], as shown in Fig. 3(b), which consists of 32 resistors R_p. The resistance of R_p is selected according to the upper limit of the chest measurement impedance. Thus, R_p is the resistance of 499 Ω, 0.01% precision, and temperature drift coefficient of 5 ppm.

The method of calibration is as follows.

In practical applications, the phase of the measurement channel $\emptyset$ includes not only theoretical phase offset $\emptyset_z$ caused by the measured target, but the phase deviation coefficient ε caused by system error. Therefore, the phase $\emptyset$ can be expressed as:

$$\phi = \varepsilon + \phi_z. \tag{2}$$

Meanwhile, the modulus Z is also subject to a certain degree deviation. The amplitude deviation coefficient is defined

as μ, and Z_0 is the theoretical value of the load. The expression of the modulus Z is:

$$Z = \mu \cdot Z_0. \tag{3}$$

The measured voltages at different excitation frequencies have different phases and modulus deviations owing to the existence of errors. Therefore, the real and imaginary parts of the transmission impedance obtained by the orthogonal digital demodulation method [25] are expressed as:

$$Z_{\text{re}} = \mu \cdot Z_0 \cdot \cos(\phi_z + \varepsilon), \tag{4}$$
$$Z_{im} = \mu \cdot Z_0 \cdot \sin(\phi_z + \varepsilon). \tag{5}$$

When the load of the system is resistance R, the measured real and imaginary parts of the impedance will be:

$$Z_{re} = \mu \cdot R \cdot \cos\varepsilon, \tag{6}$$
$$Z_{im} = \mu \cdot R \cdot \sin\varepsilon. \tag{7}$$

The equations for ε and μ of system's each channel at each frequency can be derived from (6) and (7) as:

$$\varepsilon = \tan^{-1}(Z_{im}/Z_{re}), \tag{8}$$
$$\mu = \sqrt{(Z_{re}^2 + Z_{im}^2)/R}. \tag{9}$$

Therefore, the theoretical phase offset $\emptyset_z$ and modulus Z_0 can be obtained by (2) and (3).

The system could be configured to the ''frequency sweep mode'' once the acquisition is initiated and switched to the internal calibration circuit for acquisition. Then, the coefficients in (8) and (9) of each channel at a specific frequency will be calculated; thus, accurate impedance information can be obtained.

C. TIMELY EXCITATION SWITCHING CONTROL

As shown in Fig. 4, each channel in the semi-parallel system measures and converts the voltage difference signal or excitation current by Analog-to-Digital converters (ADCs) under a single excitation electrode configuration simultaneously. Then the multiplexer will switch the excitation electrode combination and repeat the process 16 times to complete the acquisition of one frame data. Therefore, the acquisition

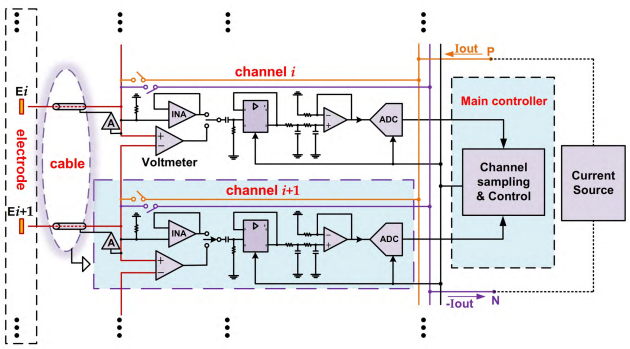

FIGURE 4. Schematic of the signal measurement module.

efficiency of the system mainly depends on the actual ADC sampling time and the settling time after excitation electrodes pair switching. The switching frequently happened when a high frame rate of the system is set, which may produce a transient response in the measuring channels owing to the presence of capacitive components in the channels and the measured target. This will not only lengthen the waiting time after the excitation switch but may affect the sampling accuracy. A method for timely controlling the switching of excitation electrode pair based on measurement voltage phase detection is proposed in this study to attenuate the transient response.

Since orthogonal sequential digital demodulation can obtain the phase information of each measurement channel in the current frame acquisition in real time and because the system's excitation current is recorded in real time [25], the phase angles θ_i between the voltages of *i-th* measurement channel and the excitation current can be obtained under each excitation electrode configuration. The *in-vivo* data pre-collection was performed without using excitation switching control to analyze the phase characteristics of the boundary voltage data in each measurement sequence. Statistic results show that the maximum phase angle in each measurement sequence is less than 25°, and the maximum absolute value of the phase difference between two consecutive frames in each measurement sequence does not change greatly (less than 0.5°). Therefore, the average values of all phase angles θ_i under each excitation electrode configuration in the previous frame were defined as the corresponding switching control factor in the current frame, which was named θ_0.

When the system needs to perform excitation electrode switching, the system controls the switching of the excitation electrode pair once the phase of the excitation current signal is the corresponding θ_0, rendering the phase of all measurement channels nearly zero at the time of excitation switching. Thus, the magnitude of the transient response is reduced, shortening the latency of the steady state in each measurement channel and the errors that may be introduced by sampling during this period.

D. HIGHLY PARALLEL FAST SAMPLING

To reduce the actual ADC sampling time, the acquisition timing of one frame data is precisely controlled (Table 1). Taking the commonly used acquisition frame rate of 100 fps and the excitation frequency of 50 kHz for instance; The system firstly triggers a delay T_w consumes 0.2 ms to ensure the completion of parameter configuration such as excitation amplitude, frequency, and gain. Since the sampling rate of the AD7986 (Analog Devices, USA) is 2 MSPS, the coherent sampling technique, which utilizes multiple periodic sampling and combines sampling points into one cycle, was adopted in ADC sampling [36]. In this case, 14 cycles of 50 kHz sine waves are sampled with equal sampling intervals and then splicing is performed to obtain two complete cycles of 256 sample points in T_{sa}, which consumes 0.28 ms.

TABLE 1. Detailed acquisition process for one frame data when excitation frequency is 50 kHz at 100 frames per second.

Process	Duration of procedure			Total time of one frame
Delay before sampling	$T_w = 0.2$ ms			$T_c = T_w + T_f + T_{id}$ = 10 ms
Drive electrodes configuration 1	$T_{sa1} = 0.28$ ms $T_{sw1} = 0.06$ ms	$T_{m1} = T_{sa1} + T_{sw1} = 0.34$ms	$T_f = 15 * T_m + T_{sa}$ = 5.38 ms	
Drive electrodes configuration 2	$T_{sa2} = 0.28$ ms $T_{sw2} = 0.06$ ms	$T_{m2} = T_{sa2} + T_{sw2} = 0.34$ms		
⋮	⋮	⋮		
Drive electrodes configuration 15	$T_{sa15} = 0.28$ ms $T_{sw15} = 0.06$ ms	$T_{m15} = T_{sa15} + T_{sw15} = 0.34$ms		
Drive electrodes configuration 16	$T_{sa16} = 0.28$ ms $T_{sw16} = 0.06$ ms	$T_{m16} = T_{sa16} + T_{sw16} = 0.34$ms		
Idle time	$T_{id} = 4.42$ ms			

The system reserves an interval T_{sw} to wait for the transient response caused by the excitation switching to disappear, which consumes 0.06 ms. Therefore, the actual sampling time of the ADC during a single excitation electrode pair period T_m is the sum of T_{sa} and T_{sw}, which consumes 0.34 ms. The actual sampling time of the complete frame data T_f is 5.38 ms. Finally, the system reserves the idle time T_{id} to ensure that the time spent on each frame of data is the same. In this case, the duration of T_{id} is 4.42 ms.

In summary, the total time T_c representing the personal computer (PC) obtaining one frame is the sum of T_w, T_f, and T_{id}, which consumes 10 ms, and the corresponding frame rate is 100 fps. Since the actual ADC sampling time of one frame T_f consumes 5.38 ms, less than the set maximum sampling time, we deem that the system can perform sufficiently fast sampling to obtain precise data for demodulation.

III. RESULTS

The general and special performance of the system were tested on several measurement targets, which were connected to the EIT system via an electrode cable with a 1-m long shield. During tests, the excitation current amplitude was always 1 mA.

A. KEY PARAMETERS OF SYSTEM PERFORMANCE

1) PERFORMANCE OF CURRENT SOURCE

The performance of BMFCS was tested and compared with the excitation source reported by Shi *et al.* (SHICS) [24]. The variation with the frequency of the SNR of the output signal and the output impedance with or without multiplexers were compared. Both tests were conducted following the method reported by Shi *et al.* [24]. Fig. 5(a) shows the SNR of two current sources; the SNR of BMFCS is better than that of SHICS and greater than 90 dB over the entire frequency range. The output impedance of two current sources with and without multiplexers is shown in Fig. 5(b). BMFCS has an output impedance greater than 1.5 MΩ without multiplexers, and its output impedance is improved compared with that of SHICS. The output impedance of BMFCS was 1.64 MΩ at 50 kHz when the multiplexers were added.

Furthermore, a resistor model with the same topology reported by Oh *et al.* [35], as shown in Fig. 3(b), was used to evaluate the suppression effectiveness of BMFCS on the common-mode signal. As shown in Fig. 5(c), taking an example where electrode 1 and electrode 9 were treated as positive (marked as P) and negative (marked as N) excitation electrodes, respectively, six pairs of voltages in two channels that have the same distance to the two excitation electrodes were marked as V_{Pj} and V_{Nj}. In this way, 16 sets of paired voltages when the positive excitation electrode is k were recorded, and the root-mean-square of voltages differences were calculated. The global paired voltage difference RMS_{CM} was defined as:

$$RMS_{CM} = \frac{1}{16}\sum_{k=1}^{16}\sqrt{\frac{1}{6}\sum_{j=1}^{6}\left(\frac{|V_{Pj}| - |V_{Nj}|}{|V_{Pj}|}\right)^2}. \quad (10)$$

Fig. 5(d) shows the RMS_{CM} variation with frequency. The measurement channels' mean square error of BMFCS is significantly smaller than that of SHICS, which means BMFCS achieves a better effect on the suppression of the common-mode signal.

2) CALIBRATION EFFECTIVENESS AND SYSTEM SNR USING THE RESISTOR MODEL

Evaluations of the calibration effectiveness and system SNR were conducted on the resistor model mentioned above.

The maximum reciprocity error (RE) and coincidence error (CE) were used to manifest the calibration effectiveness, whose definition are those used by Shi *et al.* [24]. RE is measured under the protocol of adjacent excitation, adjacent measurement, which was expressed as:

$$RE = \frac{v(c,d)\big|_{I(a,b)} - v(a,b)\big|_{I(c,d)}}{v(c,d)\big|_{I(a,b)}}. \quad (11)$$

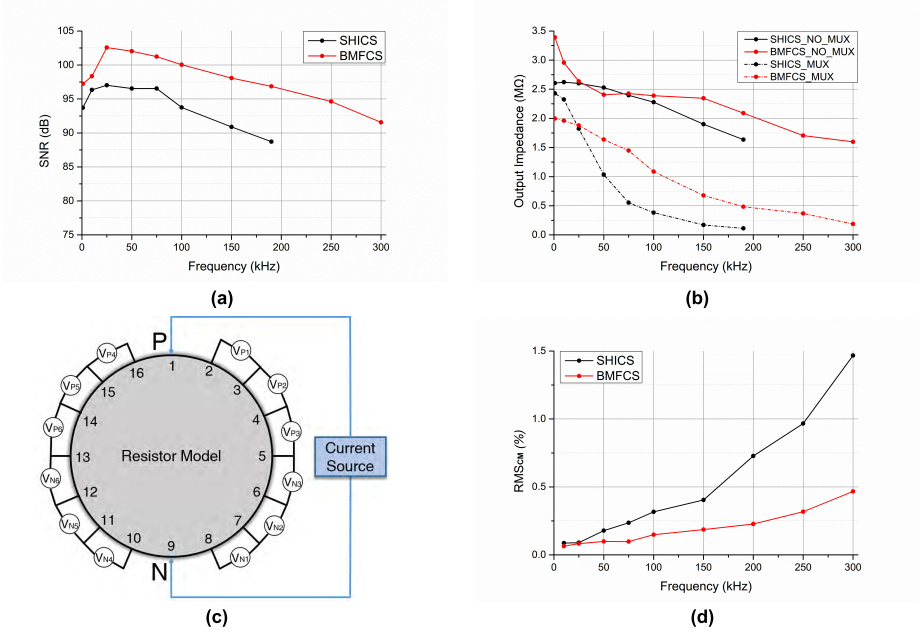

FIGURE 5. Comparisons of the bipolar-mirror feedback current source (BMFCS) and the Shi's current source (SHICS) performance [24]. (a) Signal-noise-ratio (SNR) variation with frequency. (b) Output impedance of two current sources with and without multiplexers' variation with frequency. (c) Schematic diagram of the method for suppressing the effect of the common-mode signal. (d) Global paired voltage difference (RMS_{CM}) of two current sources.

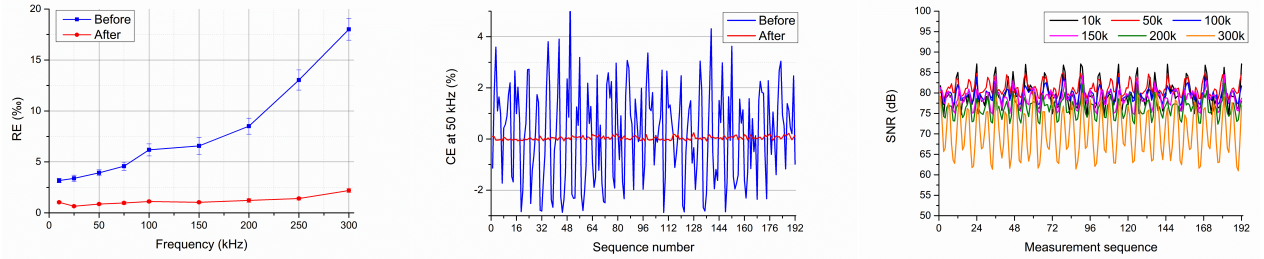

FIGURE 6. Results of calibration effectiveness and system SNR on the resistor model. (a) Comparison of reciprocity error (RE) variation with frequency before and after calibration; (b) comparison of coincidence error (CE) before and after calibration at 50 kHz; (c) SNR of system's 192 measurement sequence at different excitation frequency points.

where $v(c,d)|_{I(a,b)}$ is the voltage difference between measurement electrodes c and d while current is injected to excitation electrodes a and b. CE was calculated as:

$$CE_n = \frac{\overline{\sum_0^N V_{chn}} - V_{thn}}{V_{thn}}. \tag{12}$$

where V_{chn} and V_{thn} are the measured value and the theoretical value of the *n-th* measurement sequence respectively, and N is 6000 times measurement.

The variation of the system SNR was measured after the system had been warmed up for 15 min.
The definition of SNR was expressed as:

$$SNR_n = 20 * \log_{10}(\frac{SD(V_{chn})}{\overline{V_{chn}}}). \tag{13}$$

where $SD(V_{chn})$ is the noise amplitude, obtained using the standard deviation of the *n-th* measurement sequence, and $\overline{V_{chn}}$ is the signal amplitude, obtained using the mean value of the *n-th* measurement sequence. The data to calculate SNR at each excitation frequency point are collected in 15 min.

From Fig. 6(a), the RE decreased significantly after the internal calibration, being 0.864‰± 0.096‰at 50 kHz; the maximal RE did not exceed 2.5‰. The CE at 50 kHz is shown in Fig. 6(b), having a range of 8.49% without calibration, and an average value of 0.19%. The CE after calibration was dramatically reduced, with a range of 0.32% and an average error of 0.04%. The average SNR of all system's measurement sequence shown in Fig. 6(c) was better than 81 dB at 50 kHz.

3) EVALUATION OF TIMELY EXCITATION SWITCHING CONTROL

As shown in Fig. 7(a), a Plexiglass phantom was used to complete the assessment. The internal diameter of the phantom was 17 cm, and the height of the interior solution was 5 cm; we used a sodium chloride solution with

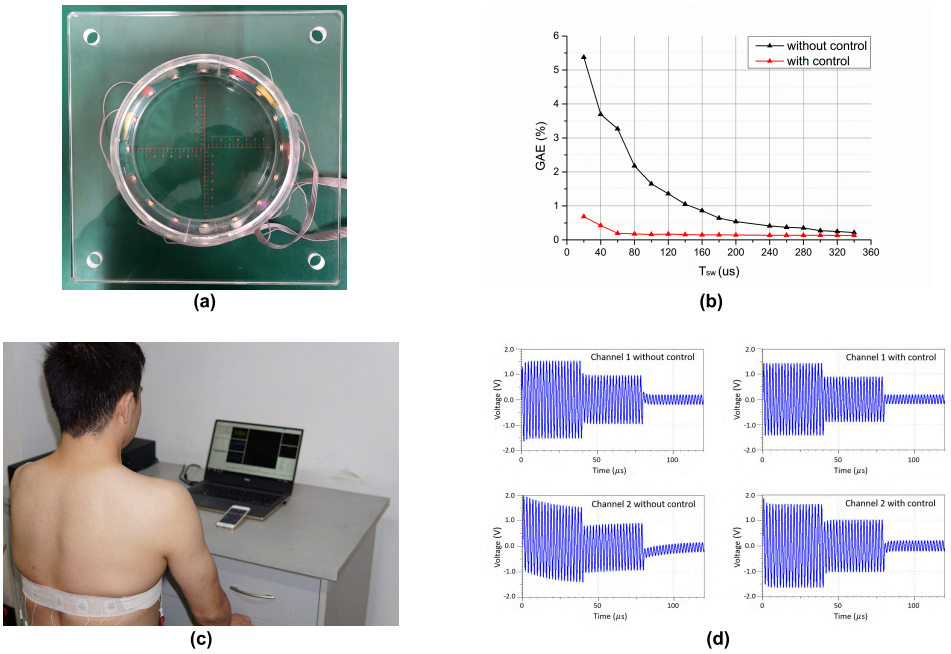

FIGURE 7. Assessment of timely excitation switching control. (a) Photo of the Plexiglass phantom. (b) Global acquisition error (GAE) with and without control on the phantom. (c) Photo of a subject in sitting position. (d) Oscilloscope records of the two voltage signals with the most apparent and slightly transient response measurement channels of in-vivo measurement and comparisons of the two channels with control and no control.

1.5 S/m conductivity. A total of 16 electrodes were equally placed on the inner wall to form an EIT sensor. The global acquisition error (GAE) was defined as the root-mean-square error of the differences between the average value of measured voltages V_{chn} in *n-th* measurement sequence and the corresponding *n-th* measured value V_{stn}. The T_{sw} in Fig. 4(b) is set to 1 ms, a value that the transient response must have completely disappeared during the period. The GAE was calculated as:

$$GAE = \frac{1}{192}\sum_{n=1}^{192}\sqrt{\left(\frac{\overline{\sum_0^N V_{chn}} - V_{stn}}{V_{stn}}\right)^2}. \qquad (14)$$

where there is almost no phase difference in each measurement channel, the GAE variation with T_{SW} at 100fps when the system is with or without switching control is shown in fig. 7(b). the GAE with switching control was much smaller than that of without control, and it maintained a low level when T_{SW} was greater than or equal to 60 us.

Then, verification of timely excitation switching control effectiveness was conducted. All experiments on human subjects were approved by the Ethics Committee of the Fourth Military Medical University [ID: FMMU-E-III-001(2-7)] and registered at Medresman.org (No. ChiCTR-DDD-16008272). As shown in Fig. 7(c), 16 silver/silver chloride electrodes were equally spaced between the fourth and fifth ribs of the chest circumference of the volunteer. The oscilloscope was used to record the voltage signals on measurement channels with and without switching control in a short continuous measurement. As shown in Fig. 7(d), channels with the most slightly and most apparent transient responses when there was no switching control were selected are compared with the signal of the same channels with switching control. The transient effect with switching control on channel 1 corresponding to the slightest transient effects was almost eliminated. Similarly, the most apparent transient effect of channel 2 was dramatically improved after switching control.

B. VERIFICATION OF SYSTEM FEASIBILITY BY BLOOD PERFUSION IMAGING

To verify the feasibility of the system design, a preliminary study of chest blood perfusion EIT imaging was conducted on a volunteer. As shown in Fig. 7(c), the subject's treatment was the same as described in section III A3. The subject took a sitting position under guidance and performed a data acquisition process of approximately 90 s. Three different ventilation states were performed throughout the test, each of which was approximately 30 s: normal breathing (NB period), inspiratory apnea (AP period), and deep breathing (DB period). The sampling frame rate was 100 fps, and the excitation current was set to 1 mA. The frequency was set to 50 kHz, which is considered to be the most robust frequency point in the bioimpedance spectrum [37]. Thus, approximately 9000 frames of data were acquired during the acquisition. At the same time, the PPG sensor was fixed to the top of the left index finger with an adhesive bandage.

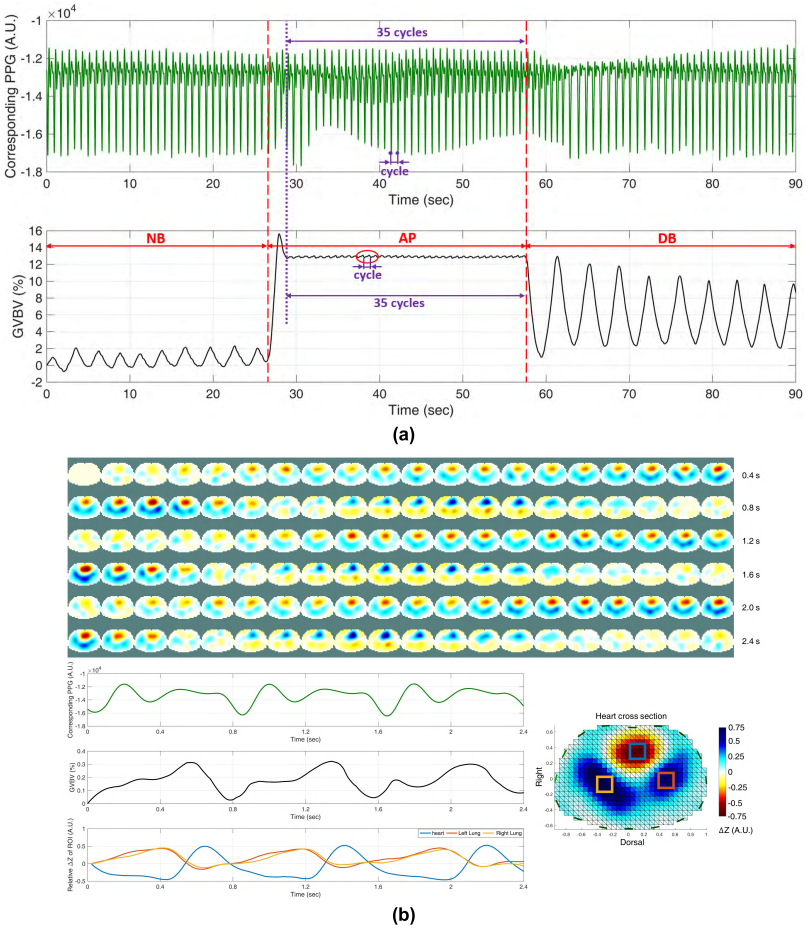

FIGURE 8. ***In-vivo*** **experiment. (a) Corresponding curves of photoplethysmography (PPG) and global variation in boundary voltages (GVBV) variations in the three lung ventilation states within the approximately 90-s test. Normal breathing (NB period), inspiratory apnea (AP period), and deep breathing (DB period). (b) EIT imaging results for the selected segment in three consecutive heartbeat cycle segments during the AP period, PPG, the variation of GVBV, and the corresponding intra-regional impedance variations of the heart, left lung, and right lung regions of interest (ROI).**

The Graz consensus Reconstruction algorithm for EIT (GREIT), a dynamic imaging algorithm proposed by Adler *et al.* [38] in 2009, was applied to reconstruct EIT images. The algorithm utilizes the reconstruction matrix with corresponding parameters to optimize image reconstruction performance, and it is implemented in the EIDORS toolbox of MATLAB R2012b (MathWorks, USA), which quickly images the acquired data as described in [39]. Since the voltage signals on the excitation electrodes cannot be accurately measured, one frame of data contains 192 valid boundary voltages, which was measured under the opposite excitation, adjacent measurement protocol. The global variation in boundary voltages (GVBV) of one frame data was defined as:

$$GVBV = \frac{1}{192} \sum_{chn=1}^{192} V_{chn}. \tag{15}$$

As shown in Fig. 8(a), the GVBV in the 90-s test was compared with the PPG variations to confirm the high correlation between them. The subject completed 86 heartbeats within 90 s, indicating that the PPG and GVBV are highly consistent. We deemed that there is a strong correlation between periodical changes in chest impedance caused by pulmonary blood perfusion and heartbeats. Therefore, the EIT data of the AP period was taken for analysis and verification. PPG and impedance data during three consecutive heartbeats [red circle in Fig. 8(a)] in the AP period were randomly selected for analysis and image reconstruction. The reference frame is the first frame of the first cycle of three consecutive cycles, thereby obtaining corresponding EIT imaging results. The first and second subfigures at the bottom of Fig. 8(b) are the PPG and GVBV variations in the selected segment. The EIT imaging results of 120 frames (every other frame was selected from a total of 240 frames) are shown at the top of Fig. 8(b), which reflect the blood flow exchanges between the heart and two lung lobes during the heartbeat cycle. To further illustrate impedance changes in the heart and lung lobes due to the perfusion cycle, three curves representing the relative

changes in the average of the impedance of the defined region of interest (ROI) marked at the right bottom of Fig. 8(b) are shown at the bottom subfigure of Fig. 8(b). The system can obtain the relevant EIT signals for the complete heartbeat cycle, and that there is a high correlation between them.

IV. DISCUSSION

Electrical impedance changes caused by blood perfusion are fast and weak, and thus require higher acquisition speed and accuracy for imaging. Therefore, fast sampling and high-precision are indispensable requirements for EIT systems to perform real-time dynamic blood perfusion imaging.

Here, a semi-parallel structure was adopted. The main control module of the system was used to perform quasi-timing sequential logic control on the parallel sampling of the ADCs, ensuring all channels under the same excitation configuration could complete the signal acquisition in a short time. Raw boundary voltage data obtained by fast sampling makes real-time processing difficult if it is directly transmitted to the PC. Therefore, the FPGA of the main control module was used to demodulate the data into modulus and phase information in real-time, thereby significantly reducing the processing burden of the PC. The system could achieve an acquisition frame rate of 100 fps, and the actual sampling time of one frame is only 5.38 ms at 50 kHz.

The traditional VCCS adopts the method of directly grounding the negative excitation electrode to release the excitation current [26]–[29]. High parasitic-capacitance generates high common-mode voltage error [30], thereby affecting the SNR of the signal and reducing the accuracy of the current output; thus, a scheme using a feedback loop to form a floating ground at both ends of the load was adopted to improve the current source used by Shi *et al.* [34]. BMFCS achieved better performance compared with SHICS, which has an SNR higher than 90 dB over the entire frequency range and an output impedance of 1.64 MΩ at 50 kHz. From Fig. 5(d), BMFCS achieves a better effect on the suppression of the common-mode signal.

A highly parallel structure will inevitably deteriorate channel consistency. Moreover, the printed circuit board (PCB) circuit, electrode leads, and stray capacitance of the human body will seriously affect the frequency response of the channel as the excitation frequency increases. To eliminate these factors, which are detrimental to the high accuracy of the system, an internal calibration unit was adopted. The calibration process operated before each acquisition can dynamically maintain the system with high measurement accuracy and channel consistency during each acquisition. Performance results show that the system can achieve RE of 0.864‰± 0.096‰at 50 kHz, and CE with a range of 0.071‰at 50 kHz after calibration. The SNR of the entire system is 81.85 dB±1.86 dB at 50 kHz, equivalent to 0.081‰± 0.019‰.

The transient response of the measuring channels when the excitation electrode pair is switched [40] must be taken into account. Massive transient response can significantly affect the acquisition accuracy of the system. In order to get an accurate measurement, the conventional method is to wait for a few more periods to allow the response to die out [35], but this method lengthens the sampling time. To minimize the transient response while ensuring that the sampling can be completed quickly, a scheme of excitation current switching control by voltage phase detection was proposed. The phase angles between the excitation current and the measured voltages were calculated in real-time. Then the system controls the switching of the excitation electrodes pair when the phases of the voltage signal in the measurement channel were nearly zero, ensuring a lower error and shorter time of the transient response. Thus, the sampling accuracy and acquisition speed are improved at the same time.

It should be noted that since the measurement target of the EIT is the human subject, the phase of each measurement channel may be different under the same excitation electrode pair, which means that the voltage signals of the 12 valid measurement channels may have different phase angles compared with the excitation signal. Therefore, the average value of the phase angles was obtained to control the switching timing of the excitation electrode pair. This is a compromise, but as can be seen from the results in Fig. 7(d), it can still significantly reduce the effect of the transient response.

A preliminary *in-vivo* experiment was designed to verify the feasibility of EIT perfusion imaging. From Fig. 8(a), when the subject performs NB, lung ventilation will cause a considerable change in lung impedance, which will be 10 times higher than the range of impedance change caused by pulmonary perfusion. This is consistent with the results of other studies [16], [41], [42], and means that the change in impedance caused by pulmonary perfusion is easily annihilated by impedance changes caused by ventilation. The impedance signal can be obtained by real-time principal component analysis, frequency domain filtering, and other methods, to obtain an independent ventilation impedance signal and perfusion impedance signal. This is based on that the frequency spectrum of the impedance change caused by lung ventilation and perfusion may be different [41], [43]. However, this is a new and novel design; the simplest and most straightforward method to verify the effectiveness of the system presented here is using the impedance signal of the subject's breath-holding state for cardiopulmonary perfusion imaging.

The results in Fig. 8 fully demonstrate that the system can reconstruct the process of injecting blood into the two lung lobes and returning the blood to the heart, which allows for more detailed analysis and interpretation. Therefore, the system provides the possibility to perform perfusion EIT imaging of other organs of the human body, such as the brain, kidney and other organs. With the aid of reference signals, EIT could help researchers and clinicians discover more valuable information about human hemodynamics, such as the monitoring of Matas training effect before carotid body tumor [44] and evaluation of renal circulatory disturbance caused by essential hypertension [45].

Although the system designed in this study exhibits excellent performance, we only conducted experiments with a healthy subject. To further assess physiological phenomena and their reproducibility and reliability, testing more subjects is necessary, and this will be our next focus. Meanwhile, in this study, a PPG sensor was fixed to the tip of the left index finger to obtain heart rate information to confirm that the period of the perfusion impedance signal change was consistent with the heartbeat period. This method is simple, but the PPG information does not provide more physiological information for analyzing the impedance information corresponding to the ROI region in Fig. 8(b). Therefore, acquiring the ECG signal as reference information may be a better choice to analysis the detailed changes in the physiological process in the future. Furthermore, studying the characteristics of human perfusion impedance signals at different frequencies to obtain more impedance information and a better quality of data is also important.

V. CONCLUSIONS

To meet the requirements of blood perfusion imaging, an EIT system utilizing several techniques to ensure high sampling rate and high precision was designed. A differential mirror VCCS, a simple and effective internal calibration, and the scheme of excitation switching control were adopted in the system. The effectiveness of these techniques and overall system performance were evaluated using several targets. A subject's thoracic pulmonary perfusion imaging experiment was conducted to assess the effectiveness of the system initially. The test and experimental results show that the designed system may provide reliable data acquisition that will help EIT perfusion imaging research in the future.

ACKNOWLEDGMENT

(Weichen Li, Junying Xia, and Ge Zhang contributed equally to this work.)

REFERENCES

[1] D. L. Thomas, M. F. Lythgoe, G. S. Pell, F. Calamante, and R. J. Ordidge, "The measurement of diffusion and perfusion in biological systems using magnetic resonance imaging," *Phys. Med. Biol.*, vol. 45, no. 8, p. R97, Aug. 2000.

[2] C. Guerin and I. Frerichs, "Getting a better picture of the correlation between lung function and structure using electrical impedance tomography," *Amer. J. Respiratory Crit. Care Med.*, vol. 190, no. 10, pp. 1186–1187, Nov. 2014.

[3] T. Robert *et al.*, "Anatomic and angiographic analyses of ophthalmic artery collaterals in moyamoya disease," *Amer. J. Neuroradiol.*, vol. 39, no. 6, pp. 1121–1126, Jun. 2018.

[4] D. Van Raemdonck, F. Rega, S. Rex, and A. Neyrinck, "Machine perfusion of thoracic organs," *J. Thoracic Disease*, vol. 10, pp. S910–S923, Apr. 2018.

[5] D.-W. Chen *et al.*, "Assessment of the cerebral hemodynamic benefits of carotid artery stenting for patients with preoperative hemodynamic impairment using cerebral single photon emission computed tomography (SPECT) and carbon dioxide inhalation," *Med. Sci. Monitor*, vol. 24, pp. 5398–5404, Aug. 2018.

[6] J. A. Detre, H. Rao, D. J. J. Wang, Y. F. Chen, and Z. Wang, "Applications of arterial spin labeled MRI in the brain," *J. Magn. Reson. Imag.*, vol. 35, no. 5, pp. 1026–1037, May 2012.

[7] L. Axel, "Cerebral blood flow determination by rapid-sequence computed tomography: Theoretical analysis," *Radiology*, vol. 137, no. 3, pp. 679–686, Dec. 1980.

[8] F. Al Badarin, A. Aljizeeri, F. Almasoudi, and M. H. Al-Mallah, "Assessment of myocardial blood flow and coronary flow reserve with positron emission tomography in ischemic heart disease: Current state and future directions," *Heart Failure Rev.*, vol. 22, no. 4, pp. 441–453, Jul. 2017.

[9] M. Wintermark *et al.*, "Comparative overview of brain perfusion imaging techniques," *Stroke*, vol. 36, no. 9, pp. e83–e99, Sep. 2005.

[10] D. S. Holder, *Electrical Impedance Tomography: Methods, History and Applications*. Boca Raton, FL, USA: CRC Press, 2004.

[11] B. H. Brown, "Electrical impedance tomography (EIT): A review," *J. Med. Eng. Technol.*, vol. 27, no. 3, pp. 97–108, May/Jun. 2003.

[12] A. Adler and A. Boyle, "Electrical impedance tomography: Tissue properties to image measures," *IEEE Trans. Biomed. Eng.*, vol. 64, no. 11, pp. 2494–2504, Nov. 2017.

[13] L. Yang *et al.*, "*In vivo* bioimpedance spectroscopy characterization of healthy, hemorrhagic and ischemic rabbit brain within 10 Hz–1 MHz," *Sensors*, vol. 17, no. 4, p. 791, Apr. 2017.

[14] A. V. Noordegraaf *et al.*, "Improvement of cardiac imaging in electrical impedance tomography by means of a new electrode configuration," *Physiolog. Meas.*, vol. 17, no. 3, pp. 88–179, Aug. 1996.

[15] S. Leonhardt and B. Lachmann, "Electrical impedance tomography: The holy grail of ventilation and perfusion monitoring?" *Intensive Care Med.*, vol. 38, no. 12, pp. 1917–1929, Dec. 2012.

[16] S. Leonhardt, R. Pikkemaat, O. Stenqvist, and S. Lundin, "Electrical impedance tomography for hemodynamic monitoring," in *Proc. Annu. Int. Conf. IEEE Eng. Med. Biol. Soc.*, Aug./Sep. 2012, pp. 122–125.

[17] G. Hahn, T. Dudykevych, I. Frerichs, and G. Hellige, "EIT System for clinical and space applications.," in *Proc. IFMBE*, vol. 3, 2002, pp. 110–111.

[18] C. A. Grant *et al.*, "Measurement of ventilation and cardiac related impedance changes with electrical impedance tomography," *Crit Care*, vol. 15, no. 1, p. R37, 2011.

[19] H. McCann, S. T. Ahsan, J. L. Davidson, R. L. Robinson, P. Wright, and C. J. D. Pomfrett, "A portable instrument for high-speed brain function imaging: FEITER," in *Proc. Annu. Int. Conf. IEEE Eng. Med. Biol. Soc.*, Aug./Sep. 2011, pp. 7029–7032.

[20] Y. Zhou and X. Li, "Multifrequency time difference EIT imaging of cardiac activities," *Biomed. Signal Process. Control*, vol. 38, pp. 128–135, Sep. 2017.

[21] R. Yerworth and R. Bayford, "The effect of serial data collection on the accuracy of electrical impedance tomography images," *Physiolog. Meas.*, vol. 34, no. 6, p. 659, Jun. 2013.

[22] R. J. Yerworth, I. Frerichs, and R. Bayford, "Analysis and compensation for errors in electrical impedance tomography images and ventilation-related measures due to serial data collection," *J. Clin. Monit. Comput.*, vol. 31, no. 5, pp. 1093–1101, Oct. 2017.

[23] T. Ouypornkochagorn, "Functional imaging of the human brain using electrical impedance tomography," Univ. Edinburgh, Edinburgh, Scotland, 2016.

[24] X. Shi *et al.*, "High-precision electrical impedance tomography data acquisition system for brain imaging," *IEEE Sensors J.*, vol. 18, no. 14, pp. 5974–5984, Jul. 2018.

[25] X. Shi, F. You, Z. Ji, F. Fu, R. Liu, and X. Dong, "Digital Demodulation in data acquisition system for multi-frequency electrical impedance tomography," in *Proc. 4th Int. Conf. Bioinf. Biomed. Eng.*, Jun. 2010, pp. 1–3.

[26] A. J. Wilson, P. Milnes, A. R. Waterworth, R. H. Smallwood, and B. H. Brown, "Mk3.5: A modular, multi-frequency successor to the Mk3a EIS/EIT system," *Physiolog. Meas.*, vol. 22, no. 1, pp. 49–54, Feb. 2001.

[27] A. McEwan, A. Romsauerova, R. Yerworth, L. Horesh, R. Bayford, and D. Holder, "Design and calibration of a compact multi-frequency EIT system for acute stroke imaging," *Physiolog. Meas.*, vol. 27, no. 5, pp. S199–S210, May 2006.

[28] M. G. Crabb *et al.*, "Mutual information as a measure of image quality for 3D dynamic lung imaging with EIT," *Physiolog. Meas.*, vol. 35, no. 5, pp. 863–879, May 2014.

[29] E. J. Lee *et al.*, "Design of a microscopic electrical impedance tomography system for 3D continuous non-destructive monitoring of tissue culture," *BioMed. Eng. OnLine*, vol. 13, p. 142, Oct. 2014.

[30] P. O. Gaggero, A. Adler, J. Brunner, and P. Seitz, "Electrical impedance tomography system based on active electrodes," *Physiolog. Meas.*, vol. 33, no. 5, pp. 831–847, May 2012.

[31] M. Rafiei-Naeini and H. McCann, "Low-noise current excitation subsystem for medical EIT," *Physiolog. Meas.*, vol. 29, no. 6, pp. S173–S184, Jun. 2008.
[32] W. C. Li *et al.*, "Research of mirror feedback current source for biological electrical impedance tomography system," *Chin. Med. Equip. J.*, vol. 36, no. 5, pp. 1–5, Feb. 2015.
[33] A. McEwan, G. Cusick, and D. S. Holder, "A review of errors in multi-frequency EIT instrumentation," *Physiolog. Meas.*, vol. 28, no. 7, pp. S197–S215, Jul. 2007.
[34] J. R. Mortarelli, "A generalization of the Geselowitz relationship useful in impedance plethysmographic field calculations," *IEEE Trans. Biomed. Eng.*, vol. BME-27, no. 11, pp. 665–667, Nov. 1980.
[35] T. I. Oh, H. Wi, D. Y. Kim, P. J. Yoo, and E. J. Woo, "A fully parallel multi-frequency EIT system with flexible electrode configuration: KHU Mark2," *Physiolog. Meas.*, vol. 32, no. 7, pp. 835–849, Jul. 2011.
[36] X. T. Shi, "Fundamental research of imaging monitoring intracranial hemorrhage using electrical impedance tomography method," Fourth Mil. Med. Univ., Xi'an, China, Tech. Rep., 2006.
[37] R. Buendia *et al.*, "Bioimpedance technology for detection of thoracic injury," *Physiolog. Meas.*, vol. 38, no. 11, pp. 2000–2014, Oct. 2017.
[38] A. Adler *et al.*, "GREIT: A unified approach to 2D linear EIT reconstruction of lung images," *Physiolog. Meas.*, vol. 30, no. 6, pp. S35–S55, Jun. 2009.
[39] A. Adler and W. R. Lionheart, "Uses and abuses of EIDORS: An extensible software base for EIT," *Physiolog. Meas.*, vol. 27, no. 5, pp. S25–S42, May 2006.
[40] M. Wang and Y. Ma, "Over-zero switching scheme for fast data collection operation in electrical impedance tomography," *Meas. Sci. Technol.*, vol. 17, no. 8, p. 2078, 2006.
[41] A. D. Leathard, B. H. Brown, J. Campbell, F. Zhang, A. H. Morice, and D. Tayler, "A comparison of ventilatory and cardiac related changes in EIT images of normal human lungs and of lungs with pulmonary emboli," *Physiolog. Meas.*, vol. 15, pp. A137–A146, May 1994.
[42] E. J. Woo, P. Hua, J. G. Webster, and W. J. Tompkins, "Measuring lung resistivity using electrical impedance tomography," *IEEE Trans. Biomed. Eng.*, vol. 39, no. 7, pp. 756–760, Jul. 1992.
[43] M. Zadehkoochak, B. H. Blott, T. K. Hames, and R. F. George, "Pulmonary perfusion and ventricular ejection imaging by frequency domain filtering of EIT images," *Clin. Phys. Physiolog. Meas.*, vol. 13, p. 191, 1992.
[44] R. Matas, "I. Testing the Efficiency of the Collateral Circulation as a Preliminary to the Occlusion of the Great Surgical Arteries," *Ann. Surg.*, vol. 53, no. 1, pp. 1–43, Jan. 1911.
[45] B. Williams, "The changing face of hypertension treatment: Treatment strategies from the 2007 ESH/ESC hypertension Guidelines," *J. Hypertension*, vol. 27, no. 3, pp. S19–S26, Jun. 2009.

WEICHEN LI received the B.S. degree in automatic control from Tianjin University, Tianjin, China, in 2012, and the M.S. degree in biomedical engineering from Fourth Military Medical University, Xi'an, China, in 2015, where he is currently pursuing the Ph.D. degree under the supervision of Prof. X. Shi. His research interests include biomedical electrical instrumentation, biomedical signal processing, and analysis of instrumentation noise.

JUNYING XIA received the B.S., M.S., and Ph.D. degrees in instrument science and technology from the National University of Defense Technology, Changsha, China, in 2004, 2006, and 2012, respectively. He is currently a Lecturer with the Department of Biomedical Engineering, Fourth Military Medical University. His current research interest includes the analysis and measurement of biological signals.

GE ZHANG received the B.S., M.S., and Ph.D. degrees in biomedical engineering from Fourth Military Medical University, Xi'an, China, in 2012, 2015, and 2018, respectively. He is currently with the Department of Radiology, Bethune International Peace Hospital.

HANG MA received the B.S. and M.S. degrees in biomedical engineering from Fourth Military Medical University, Xi'an, China, in 2013 and 2016, respectively, where he is currently pursuing the Ph.D. degree under the supervision of Prof. F. Fu. His research interest includes biosensor system design.

BENYUAN LIU was born in Shanxi, China, in 1985. He received the M.S. and Ph.D. degrees from the Science and Technology on Automatic Target Recognition Laboratory, National University of Defense Technology, Changsha, China, in 2009 and 2015, respectively. He is currently a Lecturer with the Department of Biomedical Engineering, Fourth Military Medical University. His interests include electrical impedance tomography, inverse problems, and adaptive waveform optimization.

LIN YANG received the B.S., M.S., and Ph.D. degrees in biomedical engineering from Fourth Military Medical University, Xi'an, China, in 2011, 2014, and 2017, respectively, where he is currently a Lecturer with the Department of Aerospace Medicine. His current research interest includes the algorithm of brain electrical impedance tomography.

YIMIN ZHOU received the M.S. degree from Northwestern Polytechnical University, in 2015. She is currently a Teaching Assistant with the Department of Biomedical Engineering, Fourth Military Medical University. Her research interest includes bio-electromagnetic properties.

XIUZHEN DONG (M'00) was born in China, in 1945. She received the B.S. degree in automatic control from Harbin Military Engineering University, Harbin, China, in 1968. Since 1994, she has been a Professor with Fourth Military Medical University, Xi'an, China, where she has also been a Doctoral Advisor, since 1998. She has authored or co-authored over 200 papers published in international journals and conferences. Her current research interests include electrical impedance tomography and biomedical signal detection and processing.

FENG FU received the B.S., M.S., and M.D. degrees in biomedical engineering from Fourth Military Medical University, Xi'an, China, in 1993, 1996, and 1999, respectively, where he is currently a Professor with the Department of Biomedical Engineering. His current research interest includes electrical impedance measurement and imaging.

XUETAO SHI was born in China, in 1973. He received the B.S., M.S., and Ph.D. degrees in biomedical engineering from Fourth Military Medical University, Xi'an, China, in 1995, 2001, and 2006, respectively, where he is currently a Professor with the Department of Biomedical Engineering. His current research interests include the measurement and analysis of dielectric properties of tissues, bio-impedance measurement, and imaging monitoring by electrical impedance tomography.